High spatio-temporal resolution in fMRI with 3D-EPI using cylindrical excitation and a CAIPIRINHA undersampling pattern

Authors:

Wietske van der Zwaag[12], Olivier Reynaud[2], Mayur Narsude, Daniel Gallichan[23], José P. Marques[4]

Institutions:

[1]Spinoza Centre for Neuroimaging, Amsterdam, The Netherlands

[2]Centre d'Imagerie BioMédicale, EPFL, Lausanne, Switzerland

[3]Cardiff University Brain Research Imaging Centre, Cardiff University, Cardiff, UK

[4]Donders Institute for Brain Behaviour and Cognition, Radboud University, Nijmegen, The Netherlands

Word count: 3255

Corresponding author:

W. van der Zwaag

Meibergdreef 75

1105 BK Amsterdam

the Netherlands

email: w.vanderzwaag@spinozacentre.nl

Abstract

Purpose: The combination of 3D-EPI with a 2D-CAIPIRINHA undersampling scheme provides high flexibility in the optimisation for spatial or temporal resolution. This flexibility can be further increased with the addition of a cylindrical excitation pulse, which exclusively excites the brain regions of interest. Here, 3D-EPI was combined with a 2D-RF pulse to reduce the brain area from which signal is generated, and hence, allowing either the reduction of the FOV or reduction of parallel imaging noise amplification.

Methods: 3D-EPI with cylindrical excitation and 4x3-fold undersampling in a 2D-CAIPIRINHA sampling scheme was used to generate fMRI data with 0.9mm in-plane resolution and 1.1s temporal resolution over a 5-cm diameter cylinder placed over both temporal lobes for an auditory fMRI experiment.

Results: Significant increases in image SNR and temporal SNR were found for both 2 mm^3 data and the high resolution protocol when using the cylindrical excitation pulse. Both protocols yielded highly significant BOLD responses for the presentation of natural sounds.

Conclusion: The higher tSNR of the cylindrical excitation 3D-EPI data makes this sequence an ideal choice for high spatiotemporal resolution fMRI acquisitions.

Keywords

fMRI, fast imaging, cylinder excitation, 3D-EPI, CAIPIRINHA, high resolution

Introduction

The increased BOLD sensitivity available at ultra-high field is often traded for increased spatial and temporal resolution, usually with the aid of parallel imaging acquisition techniques [1–4].
In functional MRI acquisitions with 3D-EPI, acceleration in both phase-encoding directions, but especially the slab-selection direction, leads to shorter volume TRs [5,6] and this can be highly beneficial in increasing BOLD sensitivity, as well as aid in the removal of physiological noise. The maximum parallel imaging acceleration factor generally depends on coil geometry, k-space trajectory and slice positioning. Unfolding data becomes increasingly difficult with higher acceleration factors, resulting in a g-factor penalty that is reflected in (temporal) SNR [7]. Higher undersampling factors and thus shorter TRs can be achieved with volumetric CAIPIRINHA undersampling schemes [8], which has been combined with the 3D-EPI sequence (3D-EPI-CAIPI) to achieve wholebrain coverage with 2 mm isotropic nominal spatial resolution and 500ms temporal resolution [9]. This improved detection of physiological noise has also been shown in other fast acquisition strategies, such as simultaneous multislice acquisitions using blipped CAIPIRINHA [10,11] or non-cartesian acquisitions with regularised reconstructions [12,13]. However, with any of these schemes, the spatial resolution is difficult to increase when the entire brain has to be imaged in a TR that is short enough to be compatible with BOLD fMRI. Larger matrix sizes require longer readout trains, leading to prohibitively long echo times.

One solution to the acquisition of high temporal and high spatial resolution is the use of a smaller/restricted field-of-view, covering only the specific brain regions of interest. The use of restricted field of view acquisitions has been successfully demonstrated through a combination of the standard echo planar imaging sequence with outer volume suppression methods [14,15]. One disadvantage of such implementations is that these are SAR intensive and may thus lead to increases in scan time, as well as signal loss over the non-suppressed region of interest [15]. Surface coils can also be used to avoid signal from regions that are not of interest for the experiment, but these can only be used for superficial cortical regions [16,17]. Another alternative is simply reducing the field of view and allowing aliasing within parts of the image outside the region of interest. In 3D-EPI, a 2D-RF pulse can provide a very low-SAR alternative to outer volume suppression [18], by replacing the whole brain excitation of the standard slab selection for excitation of a cylinder of freely chosen diameter and thus rendering the OVS pulses unnecessary. Using a 2D-rf pulse rather than surface coils to limit the sensitive area, the position of the excited region can be freely chosen and is thus

not limited by hardware, i.e. the positioning of the RF-coil. This means the cylinder excitation can also be used readily in difficult-to-reach areas such as the midbrain [19].

One area for which inner-volume excitation can be particularly useful is the bilateral auditory cortex in the temporal lobes. The small functional units on the temporal plane specifically require the use of high special resolution in the fMRI acquisitions [16,20–25]. Unfortunately, placing surface coils or outer volume suppression bands here can be difficult because of the bilateral position of the auditory regions.

One advantage of inner volume excitation, particularly in the context of segmented imaging, is that artefactual signal from outside the excited area will not introduce artefacts inside the region of interest [27]. For example, it could be advantageous to leave the eyeballs outside the excited region, to avoid task related eye-movement artefacts which might propagate and interfere with signal from functional regions of interest. Physiological noise contributions, which can contaminate even somewhat distant tissue if there is any Nyquist ghosting, will also be lower if those areas are placed outside the excited area. Regions to be excluded might include the large vessels surrounding the brainstem, as well as the eyes.

Exciting only a limited brain region means that a smaller FOV and matrix size can be used to acquire data with the same spatial resolution, in less time per volume. However, the same time gain can also be achieved by increasing the parallel imaging undersampling factors in a larger matrix.

In this study, we show that, using a 32-channel coil and 3D-EPI acquisition with a CAIPIRINHA undersampling scheme, a 5cm diameter cylindrical excitation can be used to achieve high (4x3) undersampling factors in a nominal wholebrain FOV image, while maintaining high image SNR as well as tSNR and hence, improved BOLD signal detection.

Methods:

All data were acquired using an actively shielded, head-only 7T MRI scanner (Siemens, Germany), equipped with a head gradient-insert (AC84, 80 mT/m max gradient strength; 350 mT/m/s slew rate) and 32-channel receive coil with tight transmit sleeve (Nova Medical, Massachusetts, USA). Eight healthy volunteers (4 females) participated in these experiments, all provided written informed consent prior to participation and the experiments were approved by the local ethics committee.

The excitation pulse of the 3D-EPI sequence [9] was replaced with a 2D-RF pulse to selectively excite a cylinder in the small flip angle regime [18,28]. The desired RF-pulse was generated using a spiral-in gradient waveform working near maximum gradient slew-rate (||S||<330 mT/m/ms) in order to minimize RF pulse duration and profile distortions. Potential slew-rate overshoots were avoided by further constraining the maximum slew-rate near the k-space center as in [29]. Placing the cylinder along the read-out axis maximized time benefits as phase encoding steps in both other axis could be reduced, or, in other words, the undersampling factors could be increased in both dimensions.
Two protocols were compared, both with a cylindrical excitation as well as with a standard slab selection excitation pulse, but otherwise identical acquisition parameters:
- a 2 mm isotropic acquisition (FOV=200 × 200 × 120 mm^3, TR = 55ms, TR_{vol} = 1.1s, TE = 27ms, α = 18°, bandwidth = 2941 Hz/pixel (echo spacing 0.44ms), GRAPPA=1x3, ΔCAIPI=2, readout gradient and cylinder along the left-right axis, cylinder radius 25 mm, alias 22 cm, Gaussian smoothing 2 mm, pulse length 3.26 ms)
- 0.9 × 0.9 × 2.0 mm^3 acquisition (FOV=200 × 200 × 120 mm^3, TR = 55ms, TR_{vol} = 1.1s, TE = 27ms, α = 18°, bandwidth = 1877 Hz/pixel (echo spacing 0.77ms), GRAPPA = 4x3, ΔCAIPI=1; same cylinder).
GRAPPA reference lines were acquired with the same excitation pulse profile used as the dataset they were acquired for. 24x48 lines were acquired for the 2 mm isotropic resolution dataset, and 96x48 lines for the 0.9 x 0.9 x 2.0 mm^3 resolution dataset. For all four datasets, the vendor-supplied online reconstruction pipeline part of the Work-in-Progress package for CAIPIRINHA was used. Raw data was additionally saved for a single subject to obtain g-factor maps.
A 0.6 mm^3 resolution MP2RAGE [30,31] dataset was acquired for anatomical reference and to aid with the placement of the cylinder centre over Heschl's gyrus in both hemispheres. The following parameters were used: matrix size: 320 × 320 × 256, FOV: 192 × 192 × 154 mm^3, $TI_1/T1_2$ = 800/2700 ms, α_1/α_2 = 4/11°. TE/TR/$TR_{MP2RAGE}$ = 3.03/7.1/6000 ms, GRAPPA = 3 and total acquisition time of 10 min. The distances from isocentre to Heschl's gyrus measured on the MP2RAGE were used as parameter inputs for the 3D-EPI sequence.

Given the importance of physiological signal contributions in 3D-EPI based acquisitions [32,33], cardiac and respiratory data were collected for physiological noise removal, along with pulse trigger events.

An auditory stimulus was used to test BOLD sensitivity in the primary auditory cortex. Presentation of 5s natural sounds, taken from [21], were alternated with 15s silence, for a total of 5 minutes. Sounds were presented using e-Prime over MR compatible headphones (Sensimetrics, Malden, MA, USA).

Data analysis

An approximate value for image SNR was obtained by dividing the mean signal in a large mid-cylinder ROI (Figure 1, blue box) by the standard deviation of the noise in an extra-cerebral ROI not affected by image artefacts. The mid-cylinder ROI was selected automatically by placing a 10.8 × 3.4 × 3.4 cm box around the centre of mass of the excited region. The noise ROI was of identical volume, placed along the image borders in the readout-direction.

Temporal SNR was calculated by dividing the temporal mean of each voxel by the temporal standard deviation of the timecourse prior to any processing steps.

G-factor maps were calculated using the general formulation for quantitative g-factor calculations in GRAPPA reconstructions [34].

fMRI data were analysed using SPM12. Standard fMRI data processing, including motion correction, smoothing with a Gaussian filter of 1.5 mm FWHM and General Linear Model (GLM) analysis, was carried out. The GLM contained a single regressor for the task-induced BOLD signal fluctuations (sound), modelled as a block convolved with the canonical hemodynamic response function (HRF), its temporal derivative, the motion parameters obtained from motion correction, physiological noise regressors as described below and three slow drift regressors. First to third order polynomials were removed from the motion parameters to reduce correlations between the two regressor sets. 10 physiological noise regressors were included: RETROICOR regressors up to second order were computed following [35], and additional regressors were added for the respiratory volume per unit of time (RVT) [36] and the cardiac rate (CR) [37]. No temporal highpass or low-pass smoothing was applied to the data.

From the activation maps, the number of voxels in the largest cluster in the primary auditory cortex region, thresholded at $p<0.05$ FWE corrected, was obtained for each hemisphere, as well as the

maximum z-score of that cluster. Paired t-tests were used to test for differences between cylindrical and slab excitation runs.

Results:

Image SNR in the 2 mm isotropic data was 36±5 % (mean ± std err over subjects) higher in the cylindrical excitation data than in the equivalent slab selection data. This improvement was further emphasized on the 0.9 mm in-plane data, where the difference increased to 45±5 %. The difference in image SNR is clear in the representative subject data shown in Figure 1, where images with equal resolution are scaled to give equal appearance to the noise in the background. Contrast in the midbrain is clearly improved for the cylindrical excitation data; the contrast the between the third ventricle, which appears bright, and the thalamus, which is darker, is much larger in the left panels than in the right ones, where the two structures can hardly be distinguished. The contrast difference might, in addition to the increased image SNR, be enhanced by differences in inflow as a smaller brain region is excited in the cylindrical excitation data.

Higher image SNR translated also into increases in tSNR values, of 29±5 % in the 2 mm^3 data and 25±1 % in the 0.9 mm in-plane data, measured again over the area indicated in Figure 1. Again, the tSNR is visibly improved in the tSNR maps for the example subject presented in Figure 2, both for the high resolution data and for the 2 mm^3 resolution data. tSNR increases were significantly higher for the medial half of the ROI than for the lateral quarters at (increases were respectively 33±5 % and 26±5 % for the 2 mm^3 data and 27±2 % and 23±1 % for the 0.9 mm in-plane data, paired t-tests $p<0.05$).

Example slices from the g-factor maps are shown in Figure 3. G-factor values within the ROI were lower, at 1.28 ± 0.16 (mean ± standard deviation), for the cylindrical excitation data than for the slab selection dataset, for which an average g-factor of 1.70±0.28 across the ROI was found.

The high tSNR led to highly significant BOLD responses in the cylindrical EPI data, an example of which is shown in Figure 4, alongside the slab selection equivalents. Across subjects, significantly ($p<0.05$) more activated voxels and a higher maximum t-score were found for the 2 mm^3 data. For the high resolution data, the differences were not significant (Table 1). The percent signal change did not differ between cylindrical excitation and slab selection data. Generally, activation was limited to the gray matter band in the 0.9 mm in-plane data, but spread somewhat across the sulci for the 2 mm^3 data. For the example subject data shown in Figure 4, positioning of the slice led to the apparent lateralisation of the BOLD responses in this example dataset, though there was no significant difference between hemispheres across subjects. Activation patterns were reproducible

between subjects and acquisition methods, although large inter-run and intersubject variability was found for the BOLD responses to this task (Table 1).

Discussion

The large tSNR gains in the cylindrical excitation data translated to gains in the number of significantly active voxels and in the maximum z-score achieved in the cylindrical excitation data (Table 1), though this difference was only significant for the 2 mm isotropic data. The percent signal change within the same region did not differ between the acquisition types, as might be expected given that the BOLD responses are expected to be identical, hence these differences in number of active voxels and maximum z-score can be attributed fully to the difference in (temporal) SNR. In the high resolution data, a similar effect size was found for the number of active voxels as for the 2 mm isotropic data (Table 1), but this difference did not reach significance ($p=0.09$). Hence, the cylindrical excitation method may not work as well with the high resolution protocol.

One of the main advantages of the 3D-EPI sequence is its flexibility in optimising the acquisition for maximum spatial or temporal resolution [5,6,9]. The cylindrical excitation pattern can add to this flexibility in two ways: A smaller excited region means a smaller imaging FOV can be used without incurring wrap-around of the peripheral brain regions. Thus, at a constant matrix size, the acquisition time per volume will be reduced, or, alternatively, provided the necessary maximum gradient strength is available, with a similar matrix size and readout time, a significantly higher spatial resolution might be achieved. However, the cylindrical excitation pattern is probably more advantageous in situations where the FOV remains unchanged, increasing the spatial or temporal resolution by an increase in the parallel imaging undersampling factor. This also leads to significantly shorter volume acquisition times and/or smaller voxel sizes and, as large parts of the imaging FOV do not contribute with any signal that needs to be unwrapped, fewer undersampling artefacts (g-factor noise amplification and residual unfolding artefacts [27]). The higher (t)SNR in the 0.9 mm in-plane cylindrical acquisition data is a direct result from this improved unfolding, as all parameters apart from the excitation profile of the pulse remained the same between cylindrical and slab selection acquisitions (Figures 1 and 2), and the g-factors were reduced (Figure 3).

Flexibility is also offered by the free placement of the cylinder, meaning that also areas difficult to reach with, for example surface coils, such as the brainstem and midbrain, can be imaged successfully as we have demonstrated in pilot studies leading to this manuscript [19]. In this study we have opted to use a general rf-pulse [28] design that excites a cylinder and whose aliasing

artifacts could be conveniently positioned outside the regions with water signal. The low tip angle needed and strong head gradients available allowed playing such an RF pulse in ~3 ms. The design of the RF pulse could be made subject specific using simple rf pulse design (thanks to the low flip angles used throughout [38]) and shortened using parallel transmit technology [39,40]. More subject specific designs using parallel transmission could ensure, for example, excitation of the hippocampus while avoiding nuisance signal coming from pulsating arteries and brain stem [41] or excitation of multiple brain regions [42]. Yet, this would come at the cost of needing to perform a transmit B1 field calibration, drawing the region of interest and designing the RF pulse while the subject is lying in the scanner.

The standard fMRI data analysis is affected in two steps by the difference between cylindrical and slab excitation: First, the cylindrical excitation could influence the amount of respiration-induced motion corrected for by the motion parameter step. Respiration induced motion does not behave as a rigid body motion (larger frequency fluctuations are found in lower slices) and by restricting the imaging volume the motion correction procedure is less driven by the brain borders and more by anatomical features of the ROI. On the other hand, severe motion could result in a change in the excited brain tissue. For none of the subjects here such motion was observed and the excited tissue contained sufficient spatial features that the quality of the motion correction was not affected by the excitation profile; as confirmed by the high tSNR values observed in the cylindrical excitation data.

And second, as any partial brain functional scan, if the brain region being scanned is small, it is highly recommended to acquire a single EPI volume with equal contrast and distortions to the functional dataset to match the partial brain to before coregistration of the anatomical scan to the functional data or vice versa. Such an extra EPI volume can be acquired in seconds and can greatly simplify the coregistration between a, distorted, T2*-weighted fMRI train with partial brain coverage and the undistorted, T1-weighted wholebrain anatomical [15].

One of the characteristics of 3D-EPI in general is the longer sampling window compared to an equivalent 2D-EPI acquisition. This leads to both higher image SNR and higher physiological noise contributions in the 3D-EPI timeseries [43,44]. While physiological noise correction can be used to remove cardiac and respiratory contributions and thus regain the SNR and BOLD sensitivity benefits of 3D-EPI [32], it might be beneficial to limit the number of segments acquired during a 3D-EPI acquisition [6]. As the use of long readout trains increases susceptibility induced distortions, the use of high parallel imaging factors to limit the length of the acquisition is expected to be more

beneficial than acquiring the same number of lines in fewer segments [9]. Here, the cylindrical excitation pulse is used to obtain a complete 3D volume in 1.1 s, with a 12-fold undersampling (4 fold in the slab direction, 3 fold in the phase-encode direction). For the 32-channel coil used, these are very high acceleration factors [45]; nevertheless excellent image quality is obtained within the cylinder at relatively low g-factors, similar to what was found by Mooiweer et al [27]. Also, the use of small, even submillimetre voxel sizes means the thermal noise component is usually much larger than the physiological noise component [46], which in turn means that physiological noise corrections at small voxel sizes only yield minimal improvements [47]. The combination of a small voxel size and relatively low number of segments afforded by the high undersampling factors yields a 3D-EPI dataset which is thus mainly thermal noise dominated.

3D-EPI CAIPI and SMS 2D-EPI blipped CAIPI sequences have various similarities both in terms of their gradient waveforms, the associated g-factor maps as has been recently shown [48] and the temporal accelerations achievable. Such inner volume excitations approaches to obtain improvements on the achievable spatial resolution will, in simultaneous multi-slice acquisitions, be limited to outer volume suppression along the phase encoding direction which is SAR prohibitive at ultrahigh fields. In the current implementation the substitution of the slab selection by the cylindrical pulse only resulted in an average increase of SAR of 17%, which remained below 3% of the SAR limit for these low-flip angle protocols.

Conclusion

In this study, we successfully used 3D-EPI with a cylindrical excitation and CAIPIRINHA undersampling scheme to acquire fMRI data with high spatio-temporal resolution and very high BOLD sensitivity. The use of a cylindrical excitation profile led to significantly higher image and temporal SNR in the target area of the functional MRI experiment, as well as improved BOLD signal detection within the cylinder for a 2-mm resolution fMRI protocol.

Acknowledgements

This work was supported by Centre d'Imagerie BioMédicale (CIBM) of the UNIL, UNIGE, HUG, CHUV, EPFL and the Leenaards and Jeantet Foundations.

Table 1

Cluster sizes, maximum z-scores and % signal change for the largest cluster located in the primary auditory cortex for cylindrical and slab selection data.

	Number voxels within the largest cluster in AI	Maximum z-score	% signal change
Slab selection, 2 mm isotropic	320 ± 100	16 ± 2	8 ± 1
Cylinder excitation, 2 mm isotropic	600 ± 100 *	21 ± 2 *	8 ± 1
Slab selection, 0.9*0.9*2 mm	390 ± 90	17 ± 1	10 ± 1
Cylinder excitation, 0.9*0.9*2 mm	630 ± 190 †	16 ± 1	10 ± 1

All data are presented as the mean ± stderr over hemispheres (16). A * indicates significant differences between the slab selection and cylindrical excitation data at $p<0.05$ (paired t-test). † indicates a tendency to difference between slab selection and cylindrical excitation data ($p<0.10$).

Figure captions

Figure 1. Example slices from a single subject. All examples are taken from a volume acquired 45s after the start of the run, from axial slices through the middle of the cylinder and sagittal slice crossing Heschl's gyrus. a): 2 mm^3 resolution, cylindrical excitation, axial slice. b) 2 mm^3 resolution, cylindrical excitation, sagittal slice. c/d): 0.9 mm in-plane data with cylindrical excitation, axial/sagittal slices. e/f) 2 mm^3 resolution, slab excitation, axial/sagittal slices. g/h) 0.9 mm in-plane with slab selection, axial/sagittal slices. The images have been scaled to give equal appearance to the noise for equal resolution. The higher signal intensity in the cylindrical excitation data is evident, for both resolutions and both in the midbrain and in the cortex. Note that also the contrast between the third ventricle around the midplain and the thalamus, which is positioned posterior and lateral to it, is improved in the cylindrical excitation volume compared to the slab selection volume, again in both the 2 mm^3 and 0.9 mm in-plane data, although it is easier to locate in the latter. The blue box in panel c indicates the region over which image SNR and temporal SNR values were obtained.

Figure 2. tSNR maps for the slices also shown in Figure 1. Maps were generated from data prior to pre-processing. Maps are scaled equally for images with the same resolution. Increases in tSNR for cylindrical excitation data are especially prominent in the central brain regions, though the cortex also shows tSNR increases.

Figure 3. Example slices from the g-factor maps for the 0.9*0.9*2 mm^3 data. The maps are scaled equally. The black square indicates the location of the ROI, centred in the cylinder. The data is from a different subject than those shown in previous Figures.

Figure 4. Activation maps from a single subject overlaid on the example slices also used in figures 1 and 2. The top row shows the 2 mm isotropic data, the bottom row the 0.9*0.9*2 mm^3 data. All activation maps are thresholded at T=5, corresponding to $p<0.05$ FWE for the 0.9 mm in-plane data. Although the 2 mm^3 data show a much larger BOLD signal change for the cylindrical excitation data, BOLD responses in the 0.9 mm in-plane data do not differ much between excitation types for this specific subject.

References

1. Van Essen DC, Ugurbil K, Auerbach E, Barch D, Behrens TEJ, Bucholz R, et al. The Human Connectome Project: a data acquisition perspective. NeuroImage. 2012;62: 2222–2231. doi:10.1016/j.neuroimage.2012.02.018

2. Polimeni JR, Fischl B, Greve DN, Wald LL. Laminar analysis of 7T BOLD using an imposed spatial activation pattern in human V1. NeuroImage. 2010;52: 1334–1346. doi:10.1016/j.neuroimage.2010.05.005

3. Satpute AB, Wager TD, Cohen-Adad J, Bianciardi M, Choi J-K, Buhle JT, et al. Identification of discrete functional subregions of the human periaqueductal gray. Proc Natl Acad Sci U S A. 2013;110: 17101–17106. doi:10.1073/pnas.1306095110

4. van der Zwaag W, Schäfer A, Marques JP, Turner R, Trampel R. Recent applications of UHF-MRI in the study of human brain function and structure: A review. 2015.

5. Poser BA, Koopmans PJ, Witzel T, Wald LL, Barth M. Three dimensional echo-planar imaging at 7 Tesla. NeuroImage. 2010;51: 261–266. doi:10.1016/j.neuroimage.2010.01.108

6. Narsude M, van der Zwaag W, Kober T, Gruetter R, Marques JP. Improved temporal resolution for functional studies with reduced number of segments with three-dimensional echo planar imaging. Magn Reson Med. 2014;72: 786–792. doi:10.1002/mrm.24975

7. Triantafyllou C, Polimeni JR, Wald LL. Physiological noise and signal-to-noise ratio in fMRI with multi-channel array coils. NeuroImage. 2011;55: 597–606. doi:10.1016/j.neuroimage.2010.11.084

8. Breuer FA, Blaimer M, Mueller MF, Seiberlich N, Heidemann RM, Griswold MA, et al. Controlled aliasing in volumetric parallel imaging (2D CAIPIRINHA). Magn Reson Med. 2006;55: 549–556. doi:10.1002/mrm.20787

9. Narsude M, Gallichan D, van der Zwaag W, Gruetter R, Marques JP. Three-dimensional echo planar imaging with controlled aliasing: A sequence for high temporal resolution functional MRI. Magn Reson Med. 2015; doi:10.1002/mrm.25835

10. Zahneisen B, Poser BA, Ernst T, Stenger AV. Simultaneous Multi-Slice fMRI using spiral trajectories. NeuroImage. 2014;92: 8–18. doi:10.1016/j.neuroimage.2014.01.056

11. Feinberg DA, Moeller S, Smith SM, Auerbach E, Ramanna S, Glasser MF, et al. Multiplexed Echo Planar Imaging for Sub-Second Whole Brain FMRI and Fast Diffusion Imaging. PLoS ONE. 2010;5: e15710. doi:10.1371/journal.pone.0015710

12. Zahneisen B, Hugger T, Lee KJ, LeVan P, Reisert M, Lee H-L, et al. Single shot concentric shells trajectories for ultra fast fMRI. Magn Reson Med. 2012;68: 484–494. doi:10.1002/mrm.23256

13. Zahneisen B, Grotz T, Lee KJ, Ohlendorf S, Reisert M, Zaitsev M, et al. Three-dimensional MR-encephalography: fast volumetric brain imaging using rosette trajectories. Magn Reson Med. 2011;65: 1260–1268. doi:10.1002/mrm.22711

14. Heidemann RM, Anwander A, Feiweier T, Knösche TR, Turner R. k-space and q-space: combining ultra-high spatial and angular resolution in diffusion imaging using ZOOPPA at 7 T. NeuroImage. 2012;60: 967–978. doi:10.1016/j.neuroimage.2011.12.081

15. van der Zwaag W, Francis S, Head K, Peters A, Gowland P, Morris P, et al. fMRI at 1.5, 3 and 7 T: characterising BOLD signal changes. NeuroImage. 2009;47: 1425–1434. doi:10.1016/j.neuroimage.2009.05.015

16. Yacoub E, Shmuel A, Logothetis N, Uğurbil K. Robust detection of ocular dominance columns in humans using Hahn Spin Echo BOLD functional MRI at 7 Tesla. NeuroImage. 2007;37: 1161–1177. doi:10.1016/j.neuroimage.2007.05.020

17. van der Zwaag W, Marques JP, Hergt M, Gruetter R. Investigation of high-resolution functional magnetic resonance imaging by means of surface and array radiofrequency coils at 7 T. Magn Reson Imaging. 2009;27: 1011–1018. doi:10.1016/j.mri.2009.01.013

18. Reynaud O, Gallichan D, Schaller B, Gruetter R. Fast low-specific absorption rate B0 -mapping along projections at high field using two-dimensional radiofrequency pulses. Magn Reson Med. 2015;73: 901–908. doi:10.1002/mrm.25217

19. van der Zwaag W, Narsude M, Reynaud O, Gallichan D, Marques JP. fast, focused fMRI at high spatial resolution: 3D-EPI-CAIPI with cylindrical excitation. ISMRM. 2015.

20. Da Costa S, Saenz M, Clarke S, van der Zwaag W. Tonotopic Gradients in Human Primary Auditory Cortex: Concurring Evidence From High-Resolution 7 T and 3 T fMRI. 2014.

21. Van der Zwaag W, Gentile G, Gruetter R, Spierer L, Clarke S. Where sound position influences sound object representations: A 7-T fMRI study. NeuroImage. 2011;54: 1803–1811. doi:10.1016/j.neuroimage.2010.10.032

22. Moerel M, De Martino F, Uğurbil K, Yacoub E, Formisano E. Processing of frequency and location in human subcortical auditory structures. Sci Rep. 2015;5: 17048. doi:10.1038/srep17048

23. Formisano E, Kim DS, Di Salle F, van de Moortele PF, Ugurbil K, Goebel R. Mirror-symmetric tonotopic maps in human primary auditory cortex. Neuron. 2003;40: 859–869.

24. Gardumi A, Ivanov D, Hausfeld L, Valente G, Formisano E, Uludağ K. The effect of spatial resolution on decoding accuracy in fMRI multivariate pattern analysis. NeuroImage. 2016;132: 32–42. doi:10.1016/j.neuroimage.2016.02.033

25. Frühholz S, van der Zwaag W, Saenz M, Belin P, Schobert A-K, Vuilleumier P, et al. Neural decoding of discriminative auditory object features depends on their socio-affective valence. Soc Cogn Affect Neurosci. 2016; doi:10.1093/scan/nsw066

26. De Martino F, Schmitter S, Moerel M, Tian J, Ugurbil K, Formisano E, et al. Spin echo functional MRI in bilateral auditory cortices at 7 T: an application of B_1 shimming. NeuroImage. 2012;63: 1313–1320. doi:10.1016/j.neuroimage.2012.08.029

27. Mooiweer R, Sbrizzi A, Raaijmakers AJE, van den Berg CAT, Luijten PR, Hoogduin H. Combining a reduced field of excitation with SENSE-based parallel imaging for maximum imaging efficiency. Magn Reson Med. 2016; doi:10.1002/mrm.26346

28. Pauly J, Nishimura D, Macovski A. A k-space analysis of small-tip-angle excitation. J Magn Reson 1969. 1989;81: 43–56. doi:10.1016/0022-2364(89)90265-5

29. Zhao T. An Improved Analytical Solution for Variable Density Spiral Design. Proc ISMRM 2008.

30. Marques JP, Kober T, Krueger G, van der Zwaag W, Van de Moortele P-F, Gruetter R. MP2RAGE, a self bias-field corrected sequence for improved segmentation and T1-mapping at high field. NeuroImage. 2010;49: 1271–1281. doi:10.1016/j.neuroimage.2009.10.002

31. O'Brien KR, Magill AW, Delacoste J, Marques JP, Kober T, Fautz H-P, et al. Dielectric pads and low- B1+ adiabatic pulses: complementary techniques to optimize structural T1 w whole-brain MP2RAGE scans at 7 tesla. J Magn Reson Imaging JMRI. 2014;40: 804–812. doi:10.1002/jmri.24435

32. Jorge J, Figueiredo P, van der Zwaag W, Marques JP. Signal fluctuations in fMRI data acquired with 2D-EPI and 3D-EPI at 7 Tesla. Magn Reson Imaging. 2013;31: 212–220. doi:10.1016/j.mri.2012.07.001

33. Lutti A, Thomas DL, Hutton C, Weiskopf N. High-resolution functional MRI at 3 T: 3D/2D echo-planar imaging with optimized physiological noise correction. Magn Reson Med. 2013;69: 1657–1664. doi:10.1002/mrm.24398

34. Breuer FA, Kannengiesser SAR, Blaimer M, Seiberlich N, Jakob PM, Griswold MA. General formulation for quantitative G-factor calculation in GRAPPA reconstructions. Magn Reson Med. 2009;62: 739–746. doi:10.1002/mrm.22066

35. Glover GH, Li TQ, Ress D. Image-based method for retrospective correction of physiological motion effects in fMRI: RETROICOR. Magn Reson Med. 2000;44: 162–167.

36. Birn RM, Smith MA, Jones TB, Bandettini PA. The respiration response function: the temporal dynamics of fMRI signal fluctuations related to changes in respiration. NeuroImage. 2008;40: 644–654. doi:10.1016/j.neuroimage.2007.11.059

37. Chang C, Cunningham JP, Glover GH. Influence of heart rate on the BOLD signal: the cardiac response function. NeuroImage. 2009;44: 857–869. doi:10.1016/j.neuroimage.2008.09.029

38. Grissom W, Yip C, Zhang Z, Stenger VA, Fessler JA, Noll DC. Spatial domain method for the design of RF pulses in multicoil parallel excitation. Magn Reson Med. 2006;56: 620–629. doi:10.1002/mrm.20978

39. Zhu Y. Parallel excitation with an array of transmit coils. Magn Reson Med. 2004;51: 775–784. doi:10.1002/mrm.20011

40. Katscher U, Börnert P, Leussler C, van den Brink JS. Transmit SENSE. Magn Reson Med. 2003;49: 144–150. doi:10.1002/mrm.10353

41. Mooiweer R, Sbrizzi A, Raaijmakers AJE, van den Berg CAT, Luijten PR, Hoogduin H. Squashing the g-factor: Ultra high scan acceleration factors in reduced Field of Excitation imaging. ISMRM. 2015.

42. Poser BA, Kaas A, Wiggins CJ, Uludağ K, Tse D. Dual Region - selective spiral pTX excitation for digit mapping in motor cortex and cerebellum. ISMRM.

43. Van Der Zwaag W, Marques JP, Kober T, Glover G, Gruetter R, Krueger G. Temporal SNR characteristics in segmented 3D-EPI at 7T. Magn Reson Med. 2012;67: 344–352. doi:10.1002/mrm.23007

44. van der Zwaag W, Jorge J, Butticaz D, Gruetter R. Physiological noise in human cerebellar fMRI. Magma N Y N. 2015;28: 485–492. doi:10.1007/s10334-015-0483-6

45. Wiggins GC, Triantafyllou C, Potthast A, Reykowski A, Nittka M, Wald LL. 32-channel 3 Tesla receive-only phased-array head coil with soccer-ball element geometry. Magn Reson Med. 2006;56: 216–223. doi:10.1002/mrm.20925

46. Bodurka J, Ye F, Petridou N, Murphy K, Bandettini PA. Mapping the MRI Voxel Volume in Which Thermal Noise Matches Physiological Noise-Implications for fMRI. NeuroImage. 2007;34: 542–549. doi:10.1016/j.neuroimage.2006.09.039

47. Hutton C, Josephs O, Stadler J, Featherstone E, Reid A, Speck O, et al. The impact of physiological noise correction on fMRI at 7T. NeuroImage. 2011;57: 101–112. doi:10.1016/j.neuroimage.2011.04.018

48. Zahneisen B, Ernst T, Poser BA. SENSE and simultaneous multislice imaging. Magn Reson Med. 2015;74: 1356–1362. doi:10.1002/mrm.25519

Figure 1

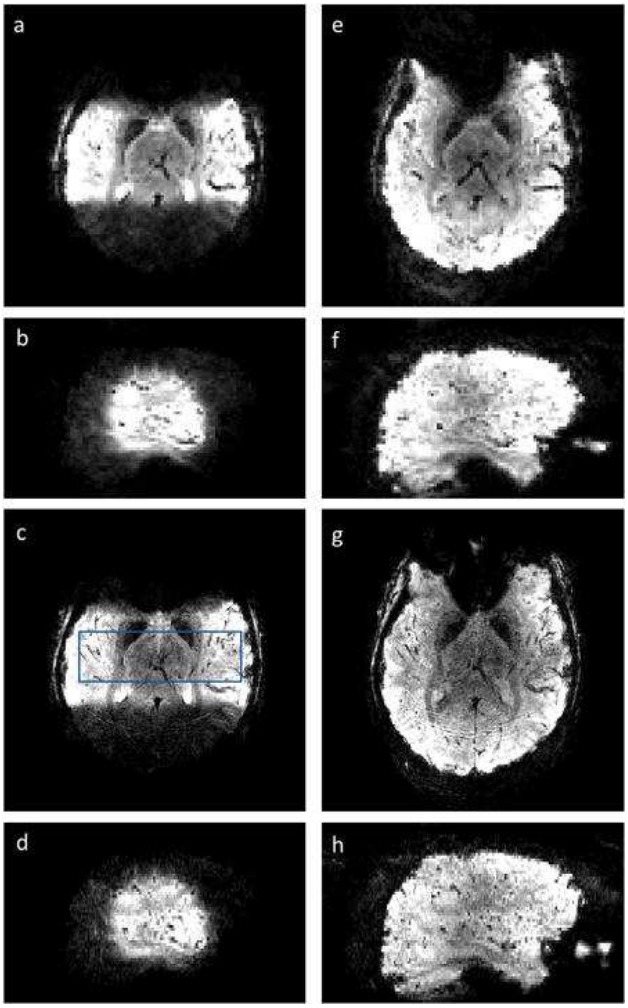

Figure 2

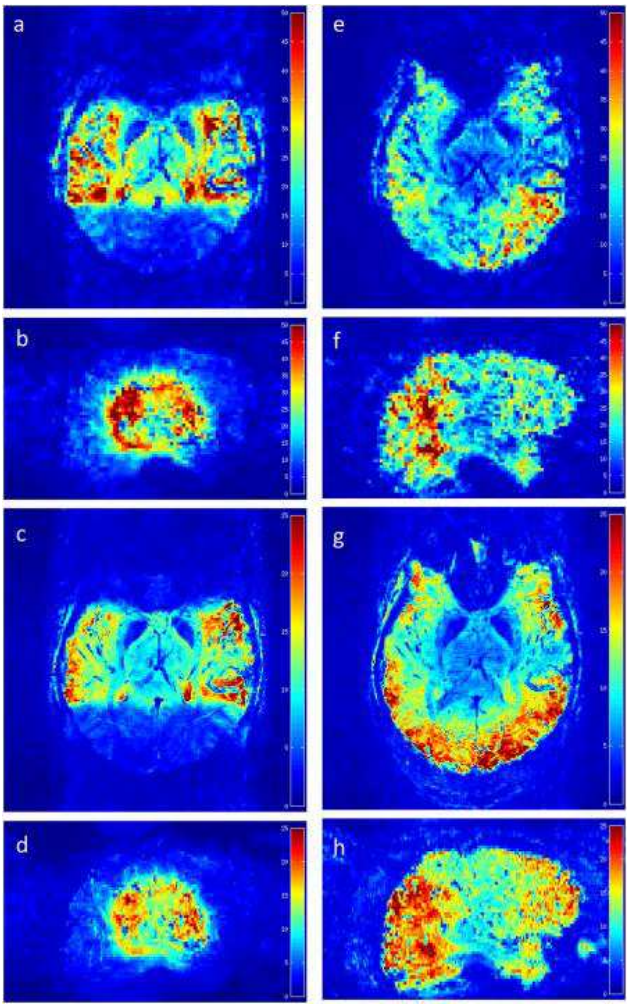

Figure 3

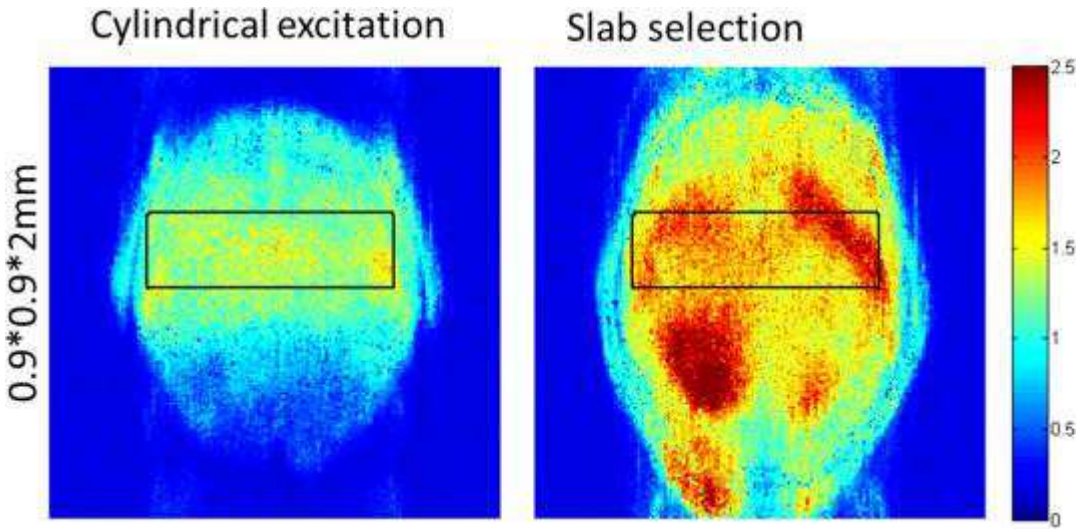

Figure 4

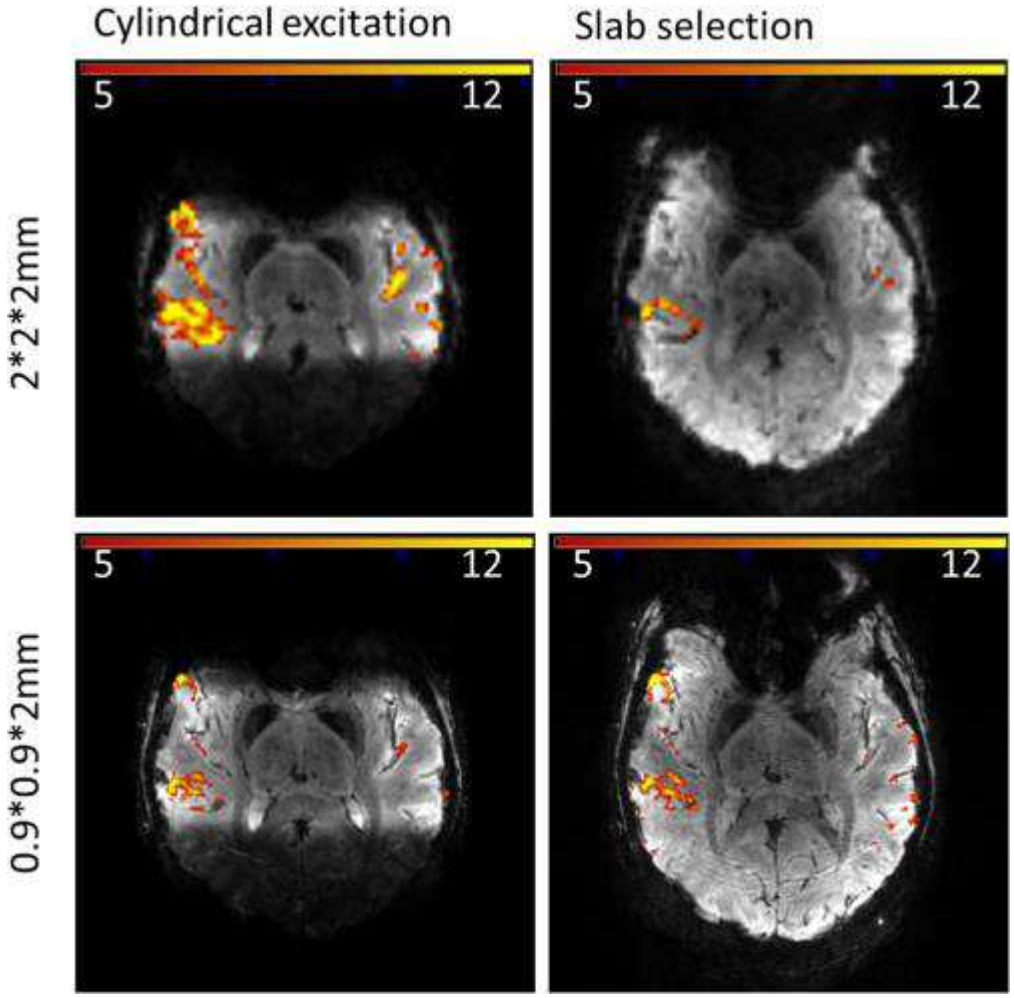
Cylindrical excitation
Slab selection
2*2*2mm
0.9*0.9*2mm
5
12
5
12
5
12
5
12